Nano Research

Open Access

Research Article

Synthesis of monolayer tungsten nitride: Rapid optical visualization and electrical impact of grain boundaries

Qiuyun Yang[1,2,§], Dehu Li[1,§], Fanfan Shi[1,§], Zhibin Shao[3], Na Wang[2], Yao Peng[1], Edwin Hang Tong Teo[4], Zheng Liu[4] ✉, and Hong Wang[1] ✉

[1] *Department of Physics, University of Science and Technology of China, Hefei 230026, China*
[2] *Institute of Electrical and Electronic Engineering, Anhui Science and Technology University, Fengyang 233100, China*
[3] *College of Mechanics and Engineering Science, Hohai University, Nanjing 211100, China*
[4] *School of Materials Science and Engineering, Nanyang Technological University, 50 Nanyang Avenue, Singapore 639798, Singapore*
[§] *Qiuyun Yang, Dehu Li, and Fanfan Shi contributed equally to this work.*

Cite this article: *Nano Research*, **2025**, *18*, 94907242. https://doi.org/10.26599/NR.2025.94907242

ABSTRACT: Two-dimensional (2D) transition metal nitrides (TMNs) have garnered significant attention in fields such as energy storage and nanoelectronics due to their unique electrical properties, high chemical stability, and excellent mechanical strength. In polycrystalline 2D TMNs films, grain boundaries (GBs) are inevitable structural defects that could play a crucial role in determining the material's properties. Developing rapid optical visualization methods is essential for obtaining large-scale information on the distribution of GBs. However, the rapid visualization of GBs in 2D TMNs, as well as the impact of GBs on the material's electrical properties, has never been previously reported. In this study, we demonstrate the growth of monolayer tungsten nitride crystals on SiO_2/Si substrates by chemical vapor deposition (CVD). High-resolution transmission electron microscopy reveals the presence of GBs at the junctions of twisted grains. A wet-etch process utilizing buffered oxide etchant (BOE) enables rapid and effective visualization of these GBs with optical microscopy. By analyzing grains with different twist angles, we find that GBs at specific angles demonstrate increased stability during etching. Electrical measurements revealed that tilted GBs hinder electrical transport, with GBs of a 62° twist angle showing sheet conductance nearly half that within the monolayer grain. This work not only provides insights into GBs in monolayer tungsten nitride but also lays the groundwork for exploring GBs-related properties in other 2D TMNs.

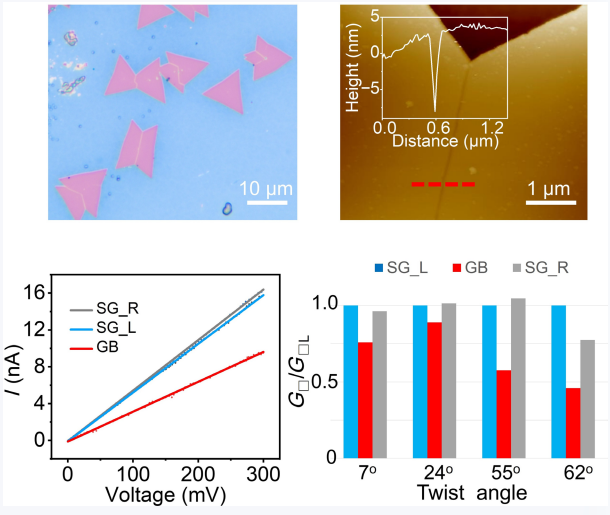

KEYWORDS: two-dimensional (2D) materials, grain boundary, chemical vapor deposition, electrical property, tungsten nitride

1 Introduction

The field of two-dimensional (2D) materials has expanded significantly with the introduction of 2D transition metal nitrides (TMNs) [1–3], which exhibit remarkable electronic [4], magnetic [5], and mechanical properties [6, 7]. These characteristics make TMNs promising candidates for diverse applications, including energy storage [8, 9], catalysis [10], and nanoelectronics [11]. For instance, the TMNs-based MXenes, a notable subset within the broader MXene family, are derived through the selective etching of layered ternary nitrides [12]. This process yields a variety of 2D TMNs characterized by specific surface chemistry and mechanical flexibility, positioning them as ideal candidates for a multitude of functional applications.

Among the various TMNs, tungsten nitride is notable for its exceptional hardness, thermal stability, and resistance to oxidation. While bulk tungsten nitride has been extensively studied and

Received: October 20, 2024; **Revised:** January 6, 2025
Accepted: January 7, 2025

✉Address correspondence to Zheng Liu, z.liu@ntu.edu.sg; Hong Wang, hwang08@ustc.edu.cn

utilized in various industrial applications such as diffusion barriers [13], research into its 2D form is still in its early stages. Monolayer or ultrathin tungsten nitride is expected to exhibit unique electronic, mechanical, and catalytic properties due to quantum confinement effects and reduced dimensionality [14, 15]. Current methods for synthesizing 2D tungsten nitride, such as molten salt-assisted synthesis methods [16–20] and chemical conversion from WS_2 nanosheets [21], primarily yield few-layer nanosheets [7, 16]. Recently, vapor–liquid–solid (VLS) growth has been used to synthesize monolayer nitrogen-rich W_5N_6 on sapphire substrates, demonstrating semimetallic properties [22]. However, this process requires a wet transfer to move the monolayer from sapphire to SiO_2/Si substrates for further characterization and application, which can introduce undesirable residues onto the sample [23]. As of now, the direct growth of monolayer tungsten nitride on SiO_2/Si substrates remains challenging.

A critical factor affecting the properties of polycrystalline 2D materials is the presence and nature of grain boundaries (GBs) [24, 25]. As has been demonstrated in other 2D materials such as graphene and MoS_2, GBs are an important type of structural defect which can significantly affect a material's electronic transport properties, mechanical strength, and chemical reactivity [24, 26–31]. Traditional techniques for visualizing GBs, such as transmission electron microscopy (TEM) and scanning tunneling microscopy (STM) [32], provide high-resolution images but are limited by the need for specialized ultrahigh vacuum equipment and inability to characterize large-area samples [33, 34]. Rapid visualization of GBs in 2D layers is an important tool to obtain the detailed information on structures such as distribution and density of GBs [33–37]. However, currently the rapid visualization of GBs in 2D tungsten nitride or other TMNs remains unexplored, thereby posing constraints on the in-depth study of GBs-related properties.

In this study, we present the growth of uniform tungsten nitride monolayer crystals on SiO_2/Si substrates using a space-confined chemical vapor deposition (CVD) method. High-resolution TEM (HRTEM) confirms the hexagonal lattice structure of the prepared samples and reveals the presence of GBs area at the junctions of twisted grains. Additionally, a simple wet-etch method is employed for rapid visualization of GBs in 2D tungsten nitride with optical microscopy. By examining grains with different twist angles, it is observed that GBs at certain twist angles exhibit greater stability during buffered oxide etchant (BOE) etching than those at other angles. Leveraging the capability to identify GBs, we perform electrical measurements both within the grain and across the GBs, revealing that GBs hinder electrical transport.

2 Results and discussion

The sample synthesis was performed in a quartz tube furnace using atmospheric pressure CVD (APCVD). Figure 1(a) schematically

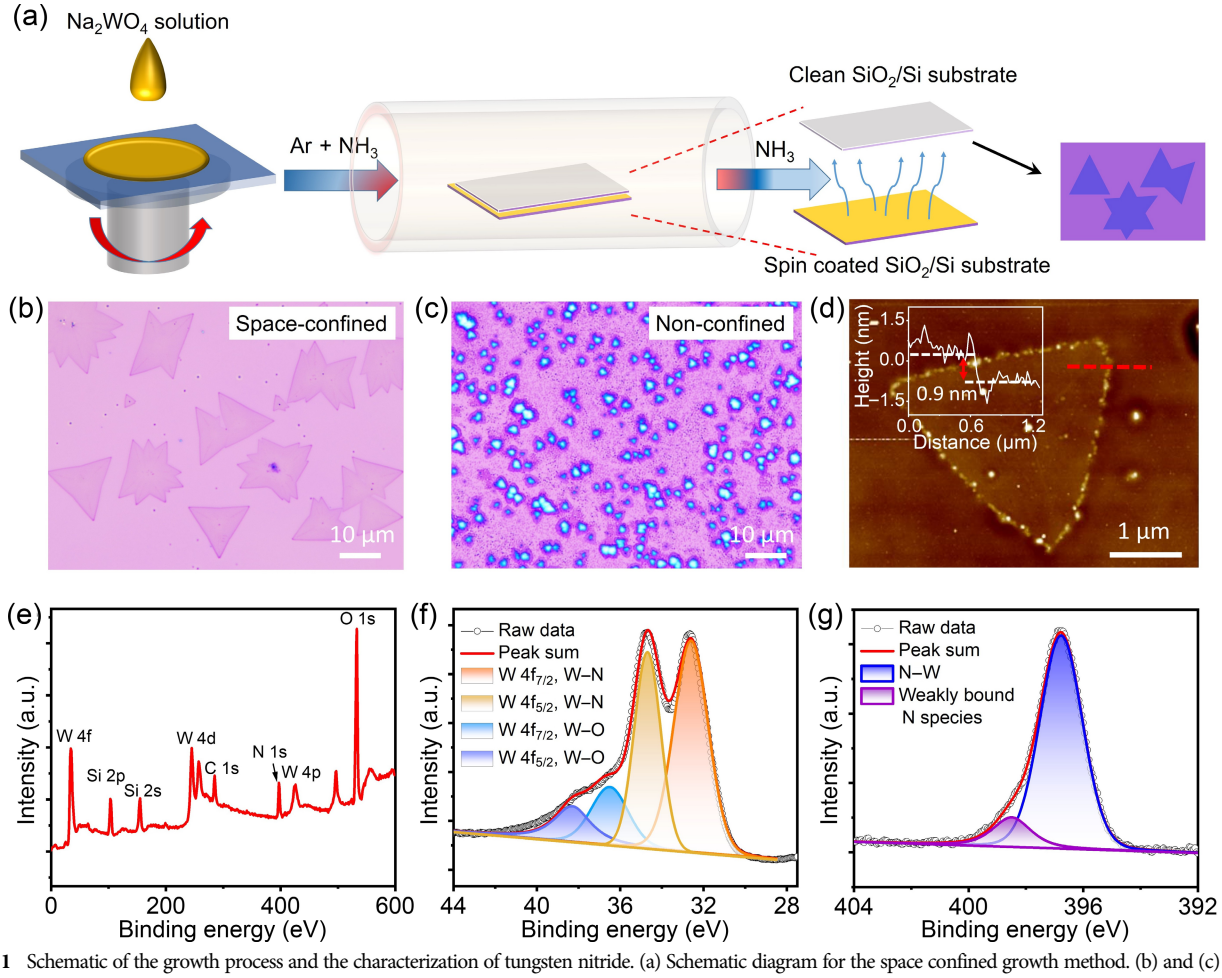

Figure 1 Schematic of the growth process and the characterization of tungsten nitride. (a) Schematic diagram for the space confined growth method. (b) and (c) Optical images of samples grown on SiO_2/Si substrates by space confined (b), and non-confined (c) growth methods, respectively. (d) AFM image of the monolayer crystal, the inset is the height profile along the red dashed line. (e)–(g) XPS survey (e), W 4f (f) and N 1s (g) spectra of ultrathin sample deposited on SiO_2/Si substrates.

illustrates the typical space-confined growth process. Sodium tungstate dihydrate ($Na_2WO_4{\cdot}2H_2O$) was used as the precursor, dissolved in a mixture of ethanol and deionized (DI) water, and then spin-coated onto SiO_2/Si substrates. The addition of ethanol enhanced the solution's wettability on the SiO_2/Si substrate and facilitated rapid solvent evaporation, aiding in the deposition of the precursor film [38]. Two SiO_2/Si substrates were placed face-to-face in the growth chamber: one spin-coated with Na_2WO_4 and the other kept clean. At the growth temperature of 820 °C, the molten Na_2WO_4 diffused onto the clean substrate and reacted with ammonia to form ultrathin tungsten nitride nuclei [39]. Due to the amorphous nature of the SiO_2/Si substrate surface [40, 41], nucleation occurs randomly. With extended growth time, these random tungsten nitride nuclei grow laterally and could merge with various twist angles.

The as-grown crystals displayed uniform color contrast on SiO_2/Si substrates (Fig. 1(b)), with monolayer crystals reaching up to 40 μm in size (Fig. S1 in the Electronic Supplementary Material (ESM)). Optical images revealed both triangular and polygonal shapes, likely due to variations during the initial nucleation stage [42]. In a control experiment without space confinement (Fig. 1(c)), the morphology and thickness of the crystals were noticeably altered, indicating that space confinement is essential for the growth of uniform monolayers [43–47]. The typical layer thickness ranged from 0.7 to 0.9 nm, as confirmed by atomic force microscopy (AFM) in Fig. 1(d) and Fig. S2 in the ESM, consistent with the thickness of a monolayer [18]. Additionally, AFM characterization of the crystal edges (Fig. S2 in the ESM) revealed discrete particles, likely resulting from impurity adsorption, giving the edges a thicker appearance compared to the interior when observed under an optical microscope. Furthermore, Fig. S3 in the ESM shows that monolayer crystals could connect to form nearly continuous films in areas with high nucleation density, demonstrating the potential of the proposed growth method for achieving large-area monolayer films on SiO_2/Si substrates. X-ray photoelectron spectroscopy (XPS) was employed to analyze the chemical states of the as-grown monolayer samples. The XPS survey spectrum in Fig. 1(e), corresponding to monolayer crystals deposited on a SiO_2/Si substrate, confirms the presence of W, Si, N, and O in the samples. The high-resolution W 4f core-level spectrum (Fig. 1(f)) reveals four distinct peaks, which correspond to nitrided W (32.6 eV for W $4f_{7/2}$ and 34.7 eV for W $4f_{5/2}$) and oxidized W (36.5 eV for W $4f_{7/2}$ and 38.3 eV for W $4f_{5/2}$) [22]. The slightly oxidized W likely forms on the surface of the tungsten nitride monolayer due to air exposure before the XPS measurement [7, 22]. Besides, the N 1s core-level spectrum was deconvoluted into two components with binding energies centered at approximately 396.7 and 398.5 eV (Fig. 1(g)). The high-intensity peak at 396.7 eV corresponds to the N–W bond, consistent with previously reported spectra for tungsten nitride films [16]. The low-intensity peak at 398.5 eV is attributed to weakly bound nitrogen or nitrogen atoms near N-vacancies [16, 48]. These weakly bound N species or N-vacancies may arise due to surface effects of the monolayer or from the low ammonia concentration used during the growth process. Thus, the XPS analysis confirms that the as-grown ultrathin crystals are tungsten nitride with N-vacancies.

To analyze the crystallographic structure, HRTEM was employed to examine both the individual triangular grain and the junction area where two grains intersect with a twisted angle. Figure 2(a) shows two merged grains transferred onto a TEM grid, with the right panel illustrating a schematic representation. The edges of the two grains slightly rolled up during the transfer process. A distinct line separating the two grains is visible in low-magnification TEM, later confirmed to be the GB. Energy-dispersive X-ray spectroscopy

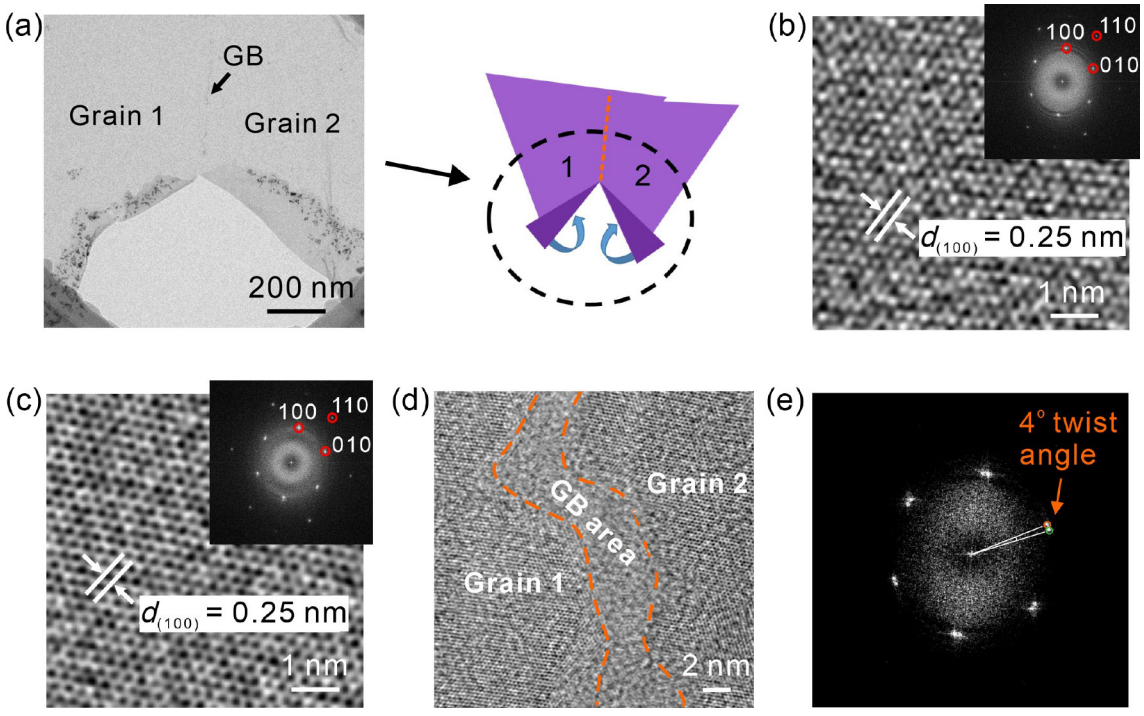

Figure 2 TEM characterizations of GBs in monolayer tungsten nitride. (a) Low-magnification TEM image of two merged grains transferred to a TEM grid. The right panel displays a schematic representation. (b) and (c) HRTEM images taken at grain 1 (b) and grain 2 (c), respectively. The insets show the corresponding FFT patterns. (d) HRTEM image taken at the region including grain 1, the dark line, and grain 2 in (a). (e) FFT pattern of (d) suggests the lattices of the two grains are twisted by a 4° angle.

(EDS) corroborates the composition of the grains, revealing that they consist of tungsten and nitrogen (Fig. S4 in the ESM). The detected oxygen is likely due to surface oxidation occurring from air exposure prior to TEM measurements. In the HRTEM image (Figs. 2(b) and 2(c)), clear lattice fringes are visible with distance of 2.5 Å, consistent with the interlayer separation (2.505 Å) of the (100) crystal plane of hexagonal W_2N_3 [16, 49]. Additionally, the 30° angle between the (100) and (110) patterns in the fast Fourier transform (FFT) images (insets of Figs. 2(b) and 2(c)) further verifies the *h*-W_2N_3 structure. This finding is supported by the X-ray diffraction (XRD) pattern (Fig. S5 in the ESM), where the main peak at 37° corresponds to the strongest (100) and (101) peaks of *h*-W_2N_3 [16]. The absence of weaker peaks is attributed to the low signal intensity of the CVD sample and interference from the amorphous SiO_2 substrate. Taking into account of the XPS analysis, the obtained sample is identified as *h*-W_2N_3 with N-vacancies.

We further investigated the dark line area shown in Fig. 2(a). Figure 2(d) presents an HRTEM image taken from the region containing grain 1, GB, and grain 2 from Fig. 2(a), revealing a distinct amorphous area that separates the highly crystalline W_2N_3 lattices. The FFT pattern of Fig. 2(d) shows two distinct hexagonal patterns with a rotation angle of 4° (Fig. 2(e)), confirming that the lattice fringes of grain 1 and grain 2 are rotated by 4°. The amorphous region observed in Fig. 2(d) is identified as the GB area. GBs, which consist of structural defects, are more susceptible to being attacked by BOE during the sample transfer process to the TEM grid. This attack likely broadens the defective GB area, transforming it from a narrow defect line into an amorphous region [50]. Due to the relatively strong interaction between the as-grown W_2N_3 and the SiO_2/Si substrate, the use of an etchant is necessary to slightly remove the SiO_2 during the transfer process for TEM sample preparation. However, SiO_2 etchants, such as HF, BOE, and KOH, even at very low concentrations, tend to attack defective GBs [51], leading to the formation of amorphous regions along the GBs. Future research is needed to develop methods for damage-free transfer of W_2N_3 GBs, enabling atomic-level characterization of the intrinsic GBs in W_2N_3 using TEM.

While TEM is capable of visualizing GBs, it requires specialized ultrahigh vacuum equipment and is not suitable for characterizing large-area samples. To address this limitation, we developed an optical microscopy-based method to rapidly visualize and locate GBs in W_2N_3 films. As illustrated in Fig. 3(a), the as-grown W_2N_3 monolayers on SiO_2/Si substrates were coated with a thin polymethyl methacrylate (PMMA) layer and then floated on a diluted BOE solution. The thin PMMA layer offers weak adhesion to the W_2N_3 films, thereby facilitating the permeation of BOE between them. As the BOE solution diffuses at the interface of PMMA and SiO_2, the SiO_2 is slightly etched. While W_2N_3 exhibits good stability in diluted BOE, the GBs—composed of various defects—can be etched by extended exposure, resulting in the formation of nanotrenches within the W_2N_3 films. These nanotrenches can be easily observed using optical microscopy once the PMMA layer is removed. Previous studies have also shown that GBs in other 2D materials, such as graphene and MoS_2, have weaker crystallinity compared to the crystal domains, making them more susceptible to etching [33, 35, 37]. Figures 3(b) and 3(c) display optical images of W_2N_3 monolayers on SiO_2/Si substrates before and after etching. The etched nanotrenches appear at the junctions where two grains merge, while no nanotrenches are found within a single triangular W_2N_3 grain, indicating the absence

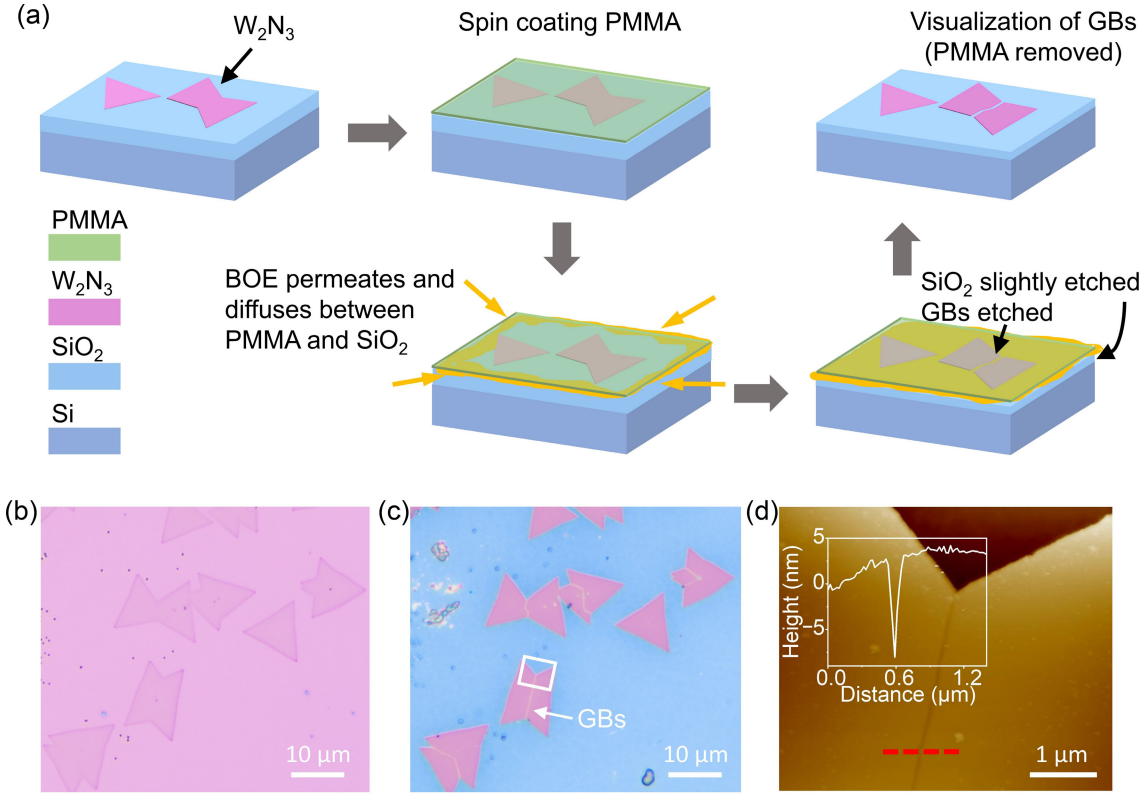

Figure 3 Visualization of GBs by optical microscopy. (a) Schematic illustration of the process for GBs visualization. (b) and (c) Optical images of the W_2N_3 grains on SiO_2/Si substrates (b) before and (c) after diluted BOE etching at room temperature. The nanotrenchs along the GBs are clearly shown after etching. (d) AFM image of the rectangular region marked in panel (c). AFM height profile (inset in panel (d)) suggests the height of the nanotrench is about 11 nm.

of GBs within individual grains (Fig. 3(c)). Figure 3(d) shows the AFM image of the marked area in Fig. 3(c). The height profile (inset of Fig. 3(d)) reveals that the height of the etched GB nanotrench is about 11 nm, which is significantly greater than the thickness of a monolayer W_2N_3. This increased height occurs because, after the GBs in W_2N_3 are etched, the underlying SiO_2 substrate is exposed to BOE and also undergoes etching. In contrast, the SiO_2 areas covered and protected by W_2N_3 are not etched by BOE, resulting in the significantly deeper nanotrenches. Furthermore, it is important to note that PMMA capping is essential for successful visualization of GBs using this etching-based method. Figure S6 in the ESM presents a comparative etching experiment of monolayer W_2N_3 with and without PMMA capping. Without PMMA capping, BOE etching proceeds rapidly and uncontrollably, often resulting in etching within the W_2N_3 grains, which is unsuitable for GBs visualization.

While the proposed etching method is destructive, it remains a valuable tool for quickly localizing and characterizing GBs over large areas, making it suitable for determining GBs density, which is crucial for understanding material properties. It is also widely accessible compared to other rapid visualization techniques, such as second-harmonic generation (SHG) or third-harmonic generation (THG), which are used in 2D MoS_2 but require sophisticated optical setups (e.g., femtosecond pulsed lasers) and nonlinear optics [25, 36]. This etching method will facilitate future extensive studies of GBs-related electrical, mechanical, and chemical properties in 2D tungsten nitride and other TMNs.

The etching behavior of GBs in W_2N_3 films was found to depend on the twist angle between adjacent grains. A diluted BOE solution (BOE:H_2O, 1:6) was used to study the evolution of GBs with time. Four typical twist angles (0°, 12°, 43°, and 60°) were selected for investigation. After 3 min of etching, GBs for 12° and 43° twist angles became visible, while no GBs were observed for the 0° and 60° samples (Figs. 4(a)–4(d)). Continued etching led to the appearance of a GB line at 60° (Fig. 4(h)) and more distinct GBs at 12° and 43° (Figs. 4(f) and 4(g)). Further, over-etching experiments (Fig. S7 in the ESM) confirm that the domains themselves were etched, as they were also not resistant when exposed to BOE after a long period. Notably, as shown in Fig. 4(e), the absence of a GB at 0° twist angle suggests that the film formed by two crystals merged at a 0° twist angle constitutes a larger single crystal. Additionally, the etching experiments indicate that GBs at the 60° twist angle are more stable during etching compared to those at other angles, with the exception of 0°. Previous studies suggest that mirror twin GBs in 60° twist-angle bicrystals of 2H-MoS_2 possess less disordered structures compared to tilt GBs [24, 52]. It is likely that the mirror twin GBs at 60° twist angle in hexagonal W_2N_3 are similarly more stable than tilt GBs, leading to a slower etching rate. Further research is necessary to elucidate the atomic structure of the 60° twist mirror twin GBs in W_2N_3.

Prior to studying the impact of GBs on the electrical properties of W_2N_3, the electrical characteristics of W_2N_3 without GBs were investigated. The devices in this study were fabricated on their original growth substrate, which may introduce potential sample-substrate coupling effects [53, 54]. Figure S8 in the ESM shows a monolayer W_2N_3 field-effect transistor (FET) device, with 285 nm SiO_2 as the dielectric layer and Si as the back gate. The transfer characteristic ($I_d - V_g$) displays almost constant drain current (I_d) with varying gate voltage (V_g), indicating the metallic behavior of the sample. Although the temperature dependence of resistance deviates from typical metallic behavior (Fig. S9 in the ESM), this is likely due to defect-participated transport [55]. The air stability of the sample was also examined through electrical and morphological characterization. As shown in Fig. S10 in the ESM, after 3 months of exposure to air, the optical morphology and AFM images of the monolayers remained almost unchanged. The surface roughness only slightly increased from 1.01 to 1.09 nm, suggesting that the sample morphology is stable in air for 3 months. For electrical properties, the resistance of the as-fabricated device was initially measured at 1.4×10^7 Ω. With air exposure, it gradually decreased and stabilized at about 0.8×10^7 Ω after 12 days (Fig. S11 in the ESM). This reduction in resistance is likely due to defect passivation, such as oxygen adsorption at vacancy sites, which reduces scattering and enhances conductivity, a phenomenon also demonstrated in monolayer MoS_2 with sulfur vacancies [56]. Further theoretical and experimental investigation is warranted to understand the interaction between air and monolayer W_2N_3 comprehensively [57, 58].

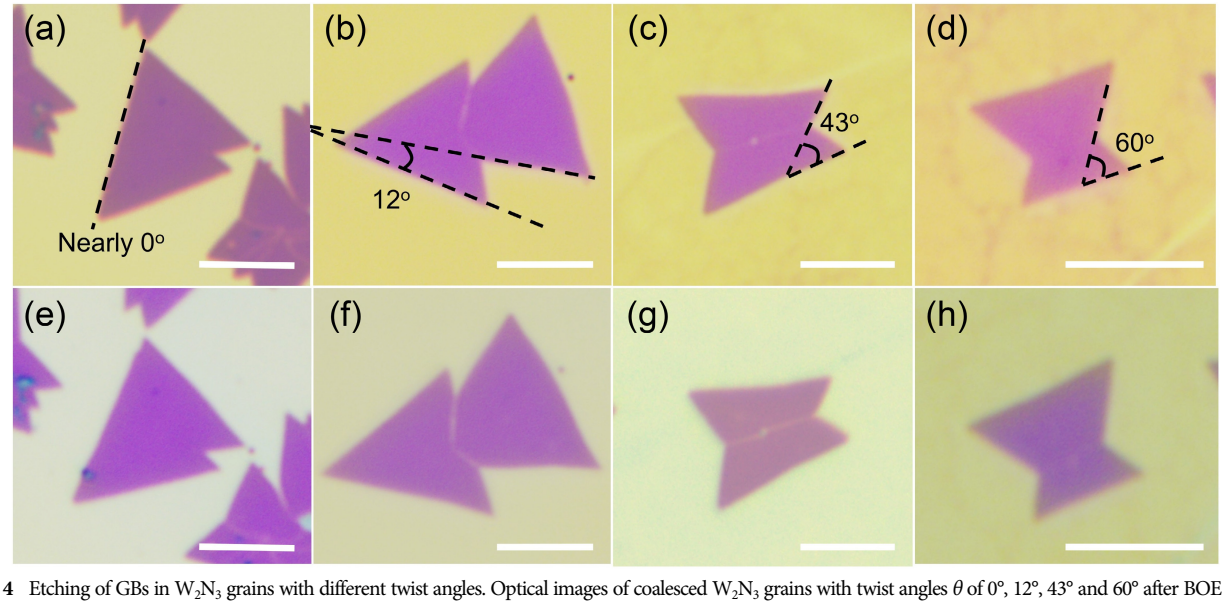

Figure 4 Etching of GBs in W_2N_3 grains with different twist angles. Optical images of coalesced W_2N_3 grains with twist angles θ of 0°, 12°, 43° and 60° after BOE etching for (a)–(d) 3 min, and (e)–(h) 6 min, respectively. The scale bars are 5 μm in all images.

To investigate the impact of a single GB on the electrical properties of monolayer W_2N_3, multi-terminal devices were fabricated using coalesced W_2N_3 grains grown on SiO_2/Si substrates. Figure 5(a) shows two triangular single crystals coalescing with a twist angle of 55°. The sample was patterned into a rectangular shape using e-beam lithography followed by reactive ion etching (RIE). Four equally spaced electrical contacts were fabricated parallel to each other and aligned along both sides of the GB, which is indicated by the red dashed line in Fig. 5(b). The single grain on the left side of the GB is labeled SG_L, and the grain on the right is labeled SG_R. A two-probe configuration was employed to measure the sheet conductance of the intra-grain regions (SG_L and SG_R) as well as the inter-grain region (across the GB). Additionally, the two-probe and four-probe methods for sheet conductance measurements of monolayer tungsten nitride were compared. As shown in Fig. S12 in the ESM, the current–voltage (I–V) curves and sheet conductance values obtained from both methods are very close, which could be attributed to the low transport barrier at the metal–sample interface. While the two-probe method may slightly underestimate the sample's conductance due to contact resistance, it is still suitable for this study since the same method was applied consistently to both intra-grain and inter-grain regions for comparative analysis.

Figure 5(c) displays the I–V curves for both the intra-grain and inter-grain regions of the device depicted in Fig. 5(b). Taking the device geometry into account, the sheet conductance, extracted from the inverse slopes of these I–V curves, are 1.4×10^{-8} S/□ for SG_L, 1.3×10^{-8} S/□ for SG_R, and 7.5×10^{-9} S/□ across the GB. The overall conductance of the W_2N_3 sample is relatively low, which could be attributed to oxygen-related surface defects or N-vacancies presented in the ultrathin monolayer W_2N_3, as suggested by the XPS measurements. However, the comparison of sheet conductance values clearly indicates that the GB region (inter-grain) is more resistive than the intra-grain regions. Furthermore, by examining additional devices made from coalesced W_2N_3 grains with twist angles of 7°, 24°, and 62° (Fig. 5(d) and Fig. S13 in the ESM), it is consistently observed that all the GBs hinder electrical transport. In some cases, the sheet conductance of the GB region is found to be nearly half of that within the W_2N_3 grain, indicating a significant suppression of electrical transport across the GB.

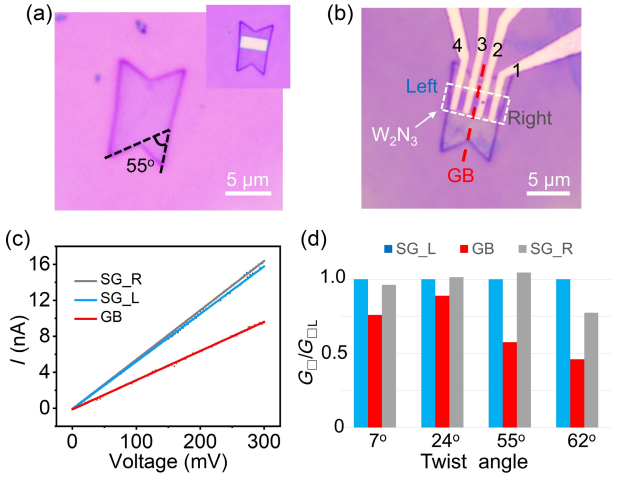

Figure 5 Impact of a single GB to the electrical properties of monolayer W_2N_3. (a) Optical image of as-grown two coalesced W_2N_3 grains with a twist angle of 55°. The inset shows the masked area before RIE etching. (b) A rectangular W_2N_3 sample containing the GB after RIE etching, contacted by four Sb/Au electrodes. The red dashed line indicates the location of the GB, which separates contacts 2 and 3. (c) Room-temperature I–V curves measured within each W_2N_3 grain (SG_R: electrode pairs 1 and 2; SG_L: electrode pairs 3 and 4) and across the GB (electrode pairs 2 and 3). (d) Comparison of the sheet conductance ratio $G_{\square}/G_{\square L}$ for the left grain (SG_L), right grain (SG_R), and the GB regions for coalesced W_2N_3 samples with twist angles of 7°, 24°, 55° and 62°. $G_{\square}$ represents sheet conductance. $G_{\square L}$ represents the sheet conductance of the left grain (SG_L).

3 Conclusions

In summary, we developed a space-confined CVD method for synthesizing monolayer tungsten nitride (W_2N_3) crystals on SiO_2/Si substrates and introduced an effective wet-etch approach for GBs visualization with optical microscopy. Our study revealed that GBs within twist grains at angles of 0° and 60° exhibit enhanced stability during etching. Electrical measurements demonstrated that W_2N_3 GBs hinder electrical conduction, serving as barriers to transport. This work provides valuable insights into the growth and characterization of monolayer W_2N_3, particularly regarding the visualization of GBs and their impact on material properties. Furthermore, it inspires further investigation into GBs-related properties across a range of other 2D TMNs.

4 Experimental

4.1 Growth of monolayer W_2N_3 crystals

Monolayer W_2N_3 was prepared using a space-confined CVD process, as illustrated in Fig. 1(a). First, sodium tungstate solution was prepared by dissolving 75 mg of sodium tungstate dihydrate ($Na_2WO_4{\cdot}2H_2O$, purity > 99%) in a mixture of 2 mL DI water and 3 mL ethanol. A 285 nm SiO_2/Si chip (1–2 cm^2) was spin-coated with the sodium tungstate solution at 3000 rpm for 1 min. Next, another clean SiO_2/Si substrate of similar size was placed face-to-face with the spin-coated substrate. Both substrates were positioned in a crucible and placed at the center of a furnace equipped with a quartz tube. The furnace was heated to 820 °C in 16 min, with 80 sccm (standard cubic centimeters per minute) of Ar as the carrier gas. Subsequently, 10 sccm of high-purity NH_3 was introduced to initiate the reaction. After 20 min of growth, the sample was rapidly cooled without altering the gas flow.

4.2 Visualization of GBs in W_2N_3

As-grown W_2N_3 monolayers on SiO_2/Si substrates were spin-coated with PMMA (6%, purchased from Hefei Vigon Material Technology Co., Ltd.) at 3000 rpm for 1 min, followed by heating on a hot plate at 130 °C for 10 min. The substrate was then cut into smaller pieces (less than 1 cm in length and width) and floated on the surface of a diluted BOE (BOE:H_2O, 1:6 to 1:4) solution. The etching time varied from 30 s to a few minutes, depending on the BOE concentration. After etching, the substrate was quickly rinsed in DI water to remove residual BOE. Finally, PMMA was removed using acetone, leaving the W_2N_3 samples adhered to the substrate, which enabled the observation of GBs under optical microscopy.

4.3 Transfer of W_2N_3 samples

For TEM measurements, the W_2N_3 sample grown on 285 nm SiO_2/Si was cut into small pieces and coated with a 950K PMMA (AllResist AR-P 672.08) film. The sample was then floated on a diluted BOE solution to slightly etch the 285 nm SiO_2 layer. Then the PMMA layer was manually detached from the substrate. Due to

the strong adhesion of AllResist PMMA (compared to Hefei Vigon), some portions of the sample adhered to the PMMA layer and were subsequently transferred to the TEM grid. This manual detachment process and the shorter exposure time of the sample to BOE resulted in less etching (compared to GBs visualization in 4.2), allowing the GBs delineation to be preserved in the TEM images. The PMMA-supported sample was rinsed several times in DI water before being picked up by a copper grid for TEM analysis. The PMMA layer was subsequently removed using acetone.

4.4 Sample characterizations

XPS spectra were collected using a Thermo Scientific ESCALAB 250Xi with monochromatic Al-Kα radiation. HRTEM and EDS images were obtained with a JEM ARM-200F operated at 200 kV. AFM images were captured using a Bruker Dimension Icon AFM in tapping mode.

4.5 Device fabrication and electrical measurements

Coalesced W_2N_3 grains with different twist angles were patterned and dry-etched into rectangular shapes using RIE (Die-RIE-Oxford-80) with SF_6/Ar. Electron beam lithography was then used to define contacts within grains and across the GBs, followed by electron beam evaporation and liftoff of Sb/Au (10 nm/30 nm). Electrical measurements were conducted using an Agilent B1500 semiconductor parameter analyzer in a probe station under vacuum. For the electrical measurements of W_2N_3 grains without GBs and the air-stability studies, Ti/Au (5 nm/30 nm) contact metals, known for their excellent air stability, were fabricated on the sample without using dry-etching processes. Measurements were primarily conducted using the two-probe method unless the four-probe method was explicitly mentioned.

Electronic Supplementary Material: Supplementary material (further details of optical images, AFM images, EDS spectrum, XRD pattern, additional electrical measurements and air stability study of the sample) is available in the online version of this article at https://doi.org/10.26599/NR.2025.94907242.

Data availability

All data needed to support the conclusions in the paper are presented in the manuscript and the Electronic Supplementary Material. Additional data related to this paper may be requested from the corresponding author upon request.

Acknowledgements

This work was supported by the National Natural Science Foundation of China (Nos. 12104434 and 62074051), and the Scientific Research Foundation of the Higher Education Institutions of Anhui Province, China (Nos. 2022AH051648 and 2024AH040057). This work was partially carried out at the University of Science and Technology of China (USTC) Center for Micro and Nanoscale Research and Fabrication.

Declaration of competing interest

All the contributing authors report no conflict of interests in this work.

Author contribution statement

Q. Y. Y.: Data curation, formal analysis, methodology, investigation, validation, writing – original draft. D. H. L.: Data curation, formal analysis, methodology, investigation, validation. F. F. S.: Data curation, formal analysis, methodology, investigation. Z. B. S.: Writing – review & editing, validation. N. W.: Investigation. Y. P.: Investigation. E. H. T. T.: Supervision, writing – review & editing. Z. L.: Supervision, project administration, writing – review & editing. H. W.: Conceptualization, methodology, project administration, supervision, validation, writing – review & editing. All the authors have approved the final manuscript.

Use of AI statement

None.

References

[1] Wang, H.; Li, J. M.; Li, K.; Lin, Y. P.; Chen, J. M.; Gao, L. J.; Nicolosi, V.; Xiao, X.; Lee, J. M. Transition metal nitrides for electrochemical energy applications. *Chem. Soc. Rev.* **2021**, *50*, 1354–1390.

[2] VahidMohammadi, A.; Rosen, J.; Gogotsi, Y. The world of two-dimensional carbides and nitrides (MXenes). *Science* **2021**, *372*, eabf1581.

[3] Fan, Y. X.; Li, L.; Zhang, Y.; Zhang, X. T.; Geng, D. C.; Hu, W. P. Recent advances in growth of transition metal carbides and nitrides (MXenes) crystals. *Adv. Funct. Mater.* **2022**, *32*, 2111357.

[4] Tang, X.; Guo, X.; Wu, W. J.; Wang, G. X. 2D metal carbides and nitrides (MXenes) as high-performance electrode materials for Lithium-based batteries. *Adv. Energy Mater.* **2018**, *8*, 1801897.

[5] Kumar, H.; Frey, N. C.; Dong, L.; Anasori, B.; Gogotsi, Y.; Shenoy, V. B. Tunable magnetism and transport properties in nitride MXenes. *ACS Nano* **2017**, *11*, 7648–7655.

[6] Hong, Y. L.; Liu, Z. B.; Wang, L.; Zhou, T. Y.; Ma, W.; Xu, C.; Feng, S.; Chen, L.; Chen, M. L.; Sun, D. M. et al. Chemical vapor deposition of layered two-dimensional $MoSi_2N_4$ materials. *Science* **2020**, *369*, 670–674.

[7] Wang, H.; Sandoz-Rosado, E. J.; Tsang, S. H.; Lin, J. J.; Zhu, M. M.; Mallick, G.; Liu, Z.; Teo, E. H. T. Elastic properties of 2D ultrathin tungsten nitride crystals grown by chemical vapor deposition. *Adv. Funct. Mater.* **2019**, *29*, 1902663.

[8] Xiao, X.; Wang, H.; Bao, W. Z.; Urbankowski, P.; Yang, L.; Yang, Y.; Maleski, K.; Cui, L. F.; Billinge, S. J. L.; Wang, G. X. et al. Two-dimensional arrays of transition metal nitride nanocrystals. *Adv. Mater.* **2019**, *31*, 1902393.

[9] Wang, D.; Zhou, C. K.; Filatov, A. S.; Cho, W.; Lagunas, F.; Wang, M. Z.; Vaikuntanathan, S.; Liu, C.; Klie, R. F.; Talapin, D. V. Direct synthesis and chemical vapor deposition of 2D carbide and nitride MXenes. *Science* **2023**, *379*, 1242–1247.

[10] Lim, K. R. G.; Handoko, A. D.; Nemani, S. K.; Wyatt, B.; Jiang, H. Y.; Tang, J. W.; Anasori, B.; Seh, Z. W. Rational design of two-dimensional transition metal carbide/nitride (MXene) hybrids and nanocomposites for catalytic energy storage and conversion. *ACS Nano* **2020**, *14*, 10834–10864.

[11] Hassan, T.; Kim, J.; Manh, H. N.; Iqbal, A.; Gao, Z. G.; Kim, H.; Hussain, N.; Naqvi, S. M.; Zaman, S.; Narayanasamy, M. et al. Semiconducting properties of delaminated titanium nitride $Ti_4N_3T_x$ MXene with gate-tunable electrical conductivity. *ACS Nano* **2024**, *18*, 23477–23488.

[12] Anasori, B.; Lukatskaya, M. R.; Gogotsi, Y. 2D metal carbides and nitrides (MXenes) for energy storage. *Nat. Rev. Mater.* **2017**, *2*, 16098.

[13] Becker, J. S.; Gordon, R. G. Diffusion barrier properties of tungsten

nitride films grown by atomic layer deposition from bis (*tert*-butylimido) bis (dimethylamido) tungsten and ammonia. *Appl. Phys. Lett.* **2003**, *82*, 2239–2241.

[14] You, J. Y.; Gu, B.; Su, G.; Feng, Y. P. Two-dimensional topological superconductivity candidate in a van der Waals layered material. *Phys. Rev. B* **2021**, *103*, 104503.

[15] Campi, D.; Kumari, S.; Marzari, N. Prediction of phonon-mediated superconductivity with high critical temperature in the two-dimensional topological semimetal W_2N_3. *Nano Lett.* **2021**, *21*, 3435–3442.

[16] Yu, H. M.; Yang, X.; Xiao, X.; Chen, M.; Zhang, Q. H.; Huang, L.; Wu, J. B.; Li, T. Q.; Chen, S. M.; Song, L. et al. Atmospheric-pressure synthesis of 2D nitrogen-rich tungsten nitride. *Adv. Mater.* **2018**, *30*, 1805655.

[17] Xiao, X.; Yu, H. M.; Jin, H. Y.; Wu, M. H.; Fang, Y. S.; Sun, J. Y.; Hu, Z. M.; Li, T. Q.; Wu, J. B.; Huang, L. et al. Salt-templated synthesis of 2D metallic MoN and other nitrides. *ACS Nano* **2017**, *11*, 2180–2186.

[18] Jin, H. Y.; Gu, Q. F.; Chen, B.; Tang, C.; Zheng, Y.; Zhang, H.; Jaroniec, M.; Qiao, S. Z. Molten salt-directed catalytic synthesis of 2D layered transition-metal nitrides for efficient hydrogen evolution. *Chem* **2020**, *6*, 2382–2394.

[19] Zhao, C. B.; Meng, C. X.; Wang, B.; Wang, C.; Li, R. T.; Fu, Q. Vapor–liquid–solid growth of thin and epitaxial transition metal nitride nanosheets for catalysis and energy conversion. *ACS Appl. Nano Mater.* **2021**, *4*, 10735–10742.

[20] Guan, H. M.; Li, W. T.; Han, J.; Yi, W. C.; Bai, H.; Kong, Q. H.; Xi, G. C. General molten-salt route to three-dimensional porous transition metal nitrides as sensitive and stable Raman substrates. *Nat. Commun.* **2021**, *12*, 1376.

[21] Cao, J.; Li, T. S.; Gao, H. Z.; Lin, Y. X.; Wang, X. Z.; Wang, H. Z.; Palacios, T.; Ling, X. Realization of 2D crystalline metal nitrides via selective atomic substitution. *Sci. Adv.* **2020**, *6*, eaax8784.

[22] Chin, H. T.; Wang, D. C.; Gulo, D. P.; Yao, Y. C.; Yeh, H. C.; Muthu, J.; Chen, D. R.; Kao, T. C.; Kalbáč, M.; Lin, P. H. et al. Tungsten nitride (W_5N_6): An ultraresilient 2D semimetal. *Nano Lett.* **2024**, *24*, 67–73.

[23] Chin, H. T.; Wang, D. C.; Wang, H.; Muthu, J.; Khurshid, F.; Chen, D. R.; Hofmann, M.; Chuang, F. C.; Hsieh, Y. P. Confined VLS growth of single-layer 2D tungsten nitrides. *ACS Appl. Mater. Interfaces* **2024**, *16*, 1705–1711.

[24] Van Der Zande, A. M.; Huang, P. Y.; Chenet, D. A.; Berkelbach, T. C.; You, Y. M.; Lee, G. H.; Heinz, T. F.; Reichman, D. R.; Muller, D. A.; Hone, J. C. Grains and grain boundaries in highly crystalline monolayer molybdenum disulphide. *Nat. Mater.* **2013**, *12*, 554–561.

[25] Yao, W. Q.; Wu, B.; Liu, Y. Q. Growth and grain boundaries in 2D materials. *ACS Nano* **2020**, *14*, 9320–9346.

[26] Ly, T. H.; Perello, D. J.; Zhao, J.; Deng, Q. M.; Kim, H.; Han, G. H.; Chae, S. H.; Jeong, H. Y.; Lee, Y. H. Misorientation-angle-dependent electrical transport across molybdenum disulfide grain boundaries. *Nat. Commun.* **2016**, *7*, 10426.

[27] Wu, J. Y.; Cao, P. Q.; Zhang, Z. S.; Ning, F. L.; Zheng, S. S.; He, J. Y.; Zhang, Z. L. Grain-size-controlled mechanical properties of polycrystalline monolayer MoS_2. *Nano Lett.* **2018**, *18*, 1543–1552.

[28] He, Y. M.; Tang, P. Y.; Hu, Z. L.; He, Q. Y.; Zhu, C.; Wang, L. Q.; Zeng, Q. S.; Golani, P.; Gao, G. H.; Fu, W. et al. Engineering grain boundaries at the 2D limit for the hydrogen evolution reaction. *Nat. Commun.* **2020**, *11*, 57.

[29] Yu, M. L.; Hu, Z. L.; Zhou, J. Z.; Lu, Y.; Guo, W. L.; Zhang, Z. H. Retrieving grain boundaries in 2D materials. *Small* **2023**, *19*, 2205593.

[30] Li, T. T.; Guo, W.; Ma, L.; Li, W. S.; Yu, Z. H.; Han, Z.; Gao, S.; Liu, L.; Fan, D. X.; Wang, Z. X. et al. Epitaxial growth of wafer-scale molybdenum disulfide semiconductor single crystals on sapphire. *Nat. Nanotechnol.* **2021**, *16*, 1201–1207.

[31] Yang, P. F.; Liu, F. C.; Li, X.; Hu, J. Y.; Zhou, F.; Zhu, L. J.; Chen, Q.; Gao, P.; Zhang, Y. F. Highly reproducible epitaxial growth of wafer-scale single-crystal monolayer MoS_2 on sapphire. *Small Methods* **2023**, *7*, 2300165.

[32] Zhao, X. X.; Ji, Y. J.; Chen, J. Y.; Fu, W.; Dan, J. D.; Liu, Y. Y.; Pennycook, S. J.; Zhou, W.; Loh, K. P. Healing of planar defects in 2D materials via grain boundary sliding. *Adv. Mater.* **2019**, *31*, 1900237.

[33] Fan, X. G.; Wagner, S.; Schädlich, P.; Speck, F.; Kataria, S.; Haraldsson, T.; Seyller, T.; Lemme, M. C.; Niklaus, F. Direct observation of grain boundaries in graphene through vapor hydrofluoric acid (VHF) exposure. *Sci. Adv.* **2018**, *4*, eaar5170.

[34] Duong, D. L.; Han, G. H.; Lee, S. M.; Gunes, F.; Kim, E. S.; Kim, S. T.; Kim, H.; Ta, Q. H.; So, K. P.; Yoon, S. J. et al. Probing graphene grain boundaries with optical microscopy. *Nature* **2012**, *490*, 235–239.

[35] Wang, J. H.; Xu, X. Z.; Qiao, R. X.; Liang, J.; Liu, C.; Zheng, B. H.; Liu, L.; Gao, P.; Jiao, Q. Z.; Yu, D. P. et al. Visualizing grain boundaries in monolayer $MoSe_2$ using mild H_2O vapor etching. *Nano Res.* **2018**, *11*, 4082–4089.

[36] Karvonen, L.; Säynätjoki, A.; Huttunen, M. J.; Autere, A.; Amirsolaimani, B.; Li, S. S.; Norwood, R. A.; Peyghambarian, N.; Lipsanen, H.; Eda, G. et al. Rapid visualization of grain boundaries in monolayer MoS_2 by multiphoton microscopy. *Nat. Commun.* **2017**, *8*, 15714.

[37] Rong, Y. M.; He, K.; Pacios, M.; Robertson, A. W.; Bhaskaran, H.; Warner, J. H. Controlled preferential oxidation of grain boundaries in monolayer tungsten disulfide for direct optical imaging. *ACS Nano* **2015**, *9*, 3695–3703.

[38] Roy, S.; Ansari, K. J.; Jampa, S. S. K.; Vutukuri, P.; Mukherjee, R. Influence of substrate wettability on the morphology of thin polymer films spin-coated on topographically patterned substrates. *ACS Appl. Mater. Interfaces* **2012**, *4*, 1887–1896.

[39] Liu, H.; Qi, G. P.; Tang, C. S.; Chen, M. L.; Chen, Y.; Shu, Z. W.; Xiang, H. Y.; Jin, Y. Y.; Wang, S. S.; Li, H. M. et al. Growth of large-area homogeneous monolayer transition-metal disulfides via a molten liquid intermediate process. *ACS Appl. Mater. Interfaces* **2020**, *12*, 13174–13181.

[40] Chae, W. H.; Cain, J. D.; Hanson, E. D.; Murthy, A. A.; Dravid, V. P. Substrate-induced strain and charge doping in CVD-grown monolayer MoS_2. *Appl. Phys. Lett.* **2017**, *111*, 143106.

[41] Sahu, R.; Radhakrishnan, D.; Vishal, B.; Negi, D. S.; Sil, A.; Narayana, C.; Datta, R. Substrate induced tuning of compressive strain and phonon modes in large area MoS_2 and WS_2 van der Waals epitaxial thin films. *J. Cryst. Growth* **2017**, *470*, 51–57.

[42] Zhang, Y.; Zhang, Y. F.; Ji, Q. Q.; Ju, J.; Yuan, H. T.; Shi, J. P.; Gao, T.; Ma, D. L.; Liu, M. X.; Chen, Y. B. et al. Controlled growth of high-quality monolayer WS_2 layers on sapphire and imaging its grain boundary. *ACS Nano* **2013**, *7*, 8963–8971.

[43] Xie, C. Y.; Jiang, S. L.; Zou, X. L.; Sun, Y. W.; Zhao, L. Y.; Hong, M.; Chen, S. L.; Huan, Y. H.; Shi, J. P.; Zhou, X. B. et al. Space-confined growth of monolayer $ReSe_2$ under a graphene layer on Au foils. *Nano Res.* **2019**, *12*, 149–157.

[44] Suleman, M.; Lee, S.; Kim, M.; Nguyen, V. H.; Riaz, M.; Nasir, N.; Kumar, S.; Park, H. M.; Jung, J.; Seo, Y. NaCl-assisted temperature-dependent controllable growth of large-area MoS_2 crystals using confined-space CVD. *ACS Omega* **2022**, *7*, 30074–30086.

[45] Li, D. W.; Xiao, Z. Y.; Mu, S.; Wang, F.; Liu, Y.; Song, J. F.; Huang, X.; Jiang, L. J.; Xiao, J.; Liu, L. et al. A facile space-confined solid-phase sulfurization strategy for growth of high-quality ultrathin molybdenum disulfide single crystals. *Nano Lett.* **2018**, *18*, 2021–2032.

[46] Zhou, S. S.; Gan, L.; Wang, D. L.; Li, H. Q.; Zhai, T. Y. Space-confined vapor deposition synthesis of two dimensional materials. *Nano Res.* **2018**, *11*, 2909–2931.

[47] Suzuki, H.; Hashimoto, R.; Misawa, M.; Liu, Y. J.; Kishibuchi, M.;

Ishimura, K.; Tsuruta, K.; Miyata, Y.; Hayashi, Y. Surface diffusion-limited growth of large and high-quality monolayer transition metal dichalcogenides in confined space of microreactor. *ACS Nano* **2022**, *16*, 11360–11373.

[48] Taborda, J. A. P.; Landázuri, H. R.; Londoño, L. P. V. Correlation between optical, morphological, and compositional properties of aluminum nitride thin films by pulsed laser deposition. *IEEE Sens. J.* **2016**, *16*, 359–364.

[49] Jin, H. Y.; Li, L. Q.; Liu, X.; Tang, C.; Xu, W. J.; Chen, S. M.; Song, L.; Zheng, Y.; Qiao, S. Z. Nitrogen vacancies on 2D layered W_2N_3: A stable and efficient active site for nitrogen reduction reaction. *Adv. Mater.* **2019**, *31*, 1902709.

[50] Chiou, B. S.; Lee, J. H. Etching of r. f. magnetron-sputtered indium tin oxide films. *J. Mater. Sci. Mater. Electron.* **1996**, *7*, 241–246.

[51] Pinto, R. M. R.; Gund, V.; Calaza, C.; Nagaraja, K. K.; Vinayakumar, K. B. Piezoelectric aluminum nitride thin-films: A review of wet and dry etching techniques. *Microelectron. Eng.* **2022**, *257*, 111753.

[52] Ahn, H.; Moon, G.; Jung, H. G.; Deng, B. C.; Yang, D. H.; Yang, S.; Han, C.; Cho, H.; Yeo, Y.; Kim, C. J. et al. Integrated 1D epitaxial mirror twin boundaries for ultrascaled 2D MoS_2 field-effect transistors. *Nat. Nanotechnol.* **2024**, *19*, 955–961.

[53] Su, L. Q.; Zhang, Y.; Yu, Y. F.; Cao, L. Y. Dependence of coupling of quasi 2-D MoS_2 with substrates on substrate types, probed by temperature dependent Raman scattering. *Nanoscale* **2014**, *6*, 4920–4927.

[54] Su, L. Q.; Yu, Y. F.; Cao, L. Y.; Zhang, Y. Effects of substrate type and material-substrate bonding on high-temperature behavior of monolayer WS_2. *Nano Res.* **2015**, *8*, 2686–2697.

[55] Anasori, B.; Shi, C. Y.; Moon, E. J.; Xie, Y.; Voigt, C. A.; Kent, P. R. C.; May, S. J.; Billinge, S. J. L.; Barsoum, M. W.; Gogotsi, Y. Control of electronic properties of 2D carbides (MXenes) by manipulating their transition metal layers. *Nanoscale Horiz.* **2016**, *1*, 227–234.

[56] Liu, Y. Y.; Stradins, P.; Wei, S. H. Air passivation of chalcogen vacancies in two-dimensional semiconductors. *Angew. Chem.* **2016**, *128*, 977–980.

[57] Grünleitner, T.; Henning, A.; Bissolo, M.; Zengerle, M.; Gregoratti, L.; Amati, M.; Zeller, P.; Eichhorn, J.; Stier, A. V.; Holleitner, A. W. et al. Real-time investigation of sulfur vacancy generation and passivation in monolayer molybdenum disulfide via *in situ* X-ray photoelectron spectromicroscopy. *ACS Nano* **2022**, *16*, 20364–20375.

[58] Bussolotti, F.; Kawai, H.; Maddumapatabandi, T. D.; Fu, W.; Khoo, K. H.; Goh, K. E. J. Role of S-vacancy concentration in air oxidation of WS_2 single crystals. *ACS Nano* **2024**, *18*, 8706–8717.